

Solar interfacial evaporation properties of carbon nanotube polyvinyl alcohol composite surface

Yifan Wang, Fengmin Su*, Yiming Fan, Yulong Ji, Nannan Zhao

Institute of Marine Engineering and Thermal Science, Dalian Maritime University, Dalian 116026, China, Tel.: +86 411 84725295; emails: fengminsu@dlmu.edu.cn (F. Su), yifanwang@dlmu.edu.cn (Y. Wang), yimingfan@dlmu.edu.cn (Y. Fan), jiyulong@dlmu.edu.cn (Y. Ji), znn@dlmu.edu.cn (N. Zhao)

Received 14 January 2023; Accepted 28 June 2023

ABSTRACT

Solar interfacial evaporation significantly improves the efficiency of solar thermal evaporation. However, if the binding strength of the light-absorbing materials to the substrate material is not sufficient, it is easy to shed under the action of external forces in practical applications and reduce the solar-thermal conversion efficiency of the evaporation surface. To solve the problem, this paper proposes a composite surface by wrapping carbon nanotubes on the surface of the cellulose sponge skeleton using polyvinyl alcohol hydrogel. Carbon nanotubes have a good light absorptivity in the wavelength range of 250–2,500 nm. Moreover, the effects of carbon nanotubes concentration, polyvinyl alcohol concentration, and water supply path area on the evaporation performance are also optimized by experiments. The results show that the transparent polyvinyl alcohol not only enhances the binding strength of carbon nanotubes but also does not reduce the light absorptivity of the evaporation surface. Under the optimal ratio of the water supply path area of 20%, at a solar irradiation intensity of $1 \text{ kW}\cdot\text{m}^{-2}$, the evaporation rate of the evaporator reaches $1.345 \pm 0.034 \text{ kg}\cdot\text{m}^{-2}\cdot\text{h}^{-1}$ with an evaporation efficiency of $89.7\% \pm 2.5\%$, evaporation performance with a long-term stability. This research provides a new method for the design and fabrication of evaporators for seawater desalination applications.

Keywords: Solar energy; Seawater desalination; Solar interfacial evaporation; Heat transfer optimization

1. Introduction

With the emergence of a series of problems such as ecological degradation, shortage of fresh water and energy, people are forced to reduce emissions and develop clean energy while pursuing economic development [1]. Traditional thermal desalination technologies rely mainly on non-renewable fossil fuels to provide heat to produce steam [2]. The excessive use of fossil fuels can cause damage to the environment and also create an energy crisis from fossil fuels [3]. Solar energy has been developed as an essential component of alternative non-renewable energy sources and in small settlements in remote areas without any hydraulic or

electric infrastructure, desalination technology driven by solar energy can become a solution to meet the water supply needs of the population [4]. Solar interfacial evaporation applies the heat converted from solar energy directly to the evaporation surface and this method has better improved energy utilization. Ghasemi et al. [5] is the first to propose the concept of solar interfacial evaporation, and achieve the light-vapor conversion efficiency of 64% at a solar irradiation intensity of $1 \text{ kW}\cdot\text{m}^{-2}$. Solar interfacial evaporation can significantly improve the efficiency of solar thermal evaporation compared with using solar energy heating bulk water to high temperatures [6]. The latest research on other novel applications of solar interfacial evaporation, such as

* Corresponding author.

combining evaporation and thermoelectricity through photothermal effects, is also a promising strategy. For example, Fan et al. [7] build a flexible solar evaporator based on MnO/C nanoparticles for simultaneous interfacial solar evaporation and thermoelectric power generation, achieving a solar-to-vapor conversion efficiency of 98.4% at a solar radiance intensity of $1 \text{ kW}\cdot\text{m}^{-2}$, and a maximum output voltage of 330 mV, an output power of 4.65 mW and a power density of $2.9 \text{ W}\cdot\text{m}^{-2}$ at a solar radiance intensity of $3 \text{ kW}\cdot\text{m}^{-2}$. Chen et al. [8] convert waste polyethylene terephthalate into porous carbon cubes, which have an evaporation rate of $2.49 \text{ kg}\cdot\text{m}^{-2}\cdot\text{h}^{-1}$ at a solar irradiation intensity of $1 \text{ kW}\cdot\text{m}^{-2}$, while producing a voltage of 201 mV and a maximum power density of $0.8 \text{ W}\cdot\text{m}^{-2}$.

Previous researchers have identified a variety of light-absorbing materials with good light-thermal conversion efficiency [9], including carbon-based materials [10,11], metal nanomaterials [12,13], and inorganic semiconductor materials [14,15], and these materials all show good photo-thermal conversion performance in solar interfacial evaporation. However, in the practical water desalination applications, the evaporator is highly susceptible to external forces such as seawater impact and extrusion, which may adversely affect the stability of light-absorbing materials, so interface stability should be considered. If the binding strength of light-absorbing materials to the water supply substrate is not sufficient, it is effortless to fall off under the action of external forces [16,17]. Which not only deteriorates the light-thermal conversion efficiency but also causes unnecessary environmental pollution. Fan et al. [18] prepares a hydrogel with interpenetrating polyvinyl alcohol and chitosan into light-absorbing material, which can promote water transport capacity and the stability of light absorbing materials. Bai et al. [19] develop synergistic photothermal materials from recycled plastics using a simple solvothermal method to construct a bifunctional Co-MOF/CNT membrane with good stability under folding and bending while achieving a high evaporation rate of $2.25 \text{ kg}\cdot\text{m}^{-2}\cdot\text{h}^{-1}$ at a solar irradiation intensity of $1 \text{ kW}\cdot\text{m}^{-2}$. Zhu et al. [20] designs flexible and washable carbon nanotubes (CNTs) embedded polyacrylonitrile non-woven fabrics by electrospinning route. Liang et al. [21] obtains the fermentation porous polyvinyl alcohol hydrogels evaporators and the activated carbon powder is fixed in it, which are soft and with satisfactory mechanical properties. Although the evaporators obtained from the above research have good interfacial stability, they all have a complex structure and require a complex pore forming process to form a porous evaporator structure.

In addition, since the temperature of the evaporation surface is higher than the ambient temperature, the solar heat absorbed by the evaporation surface inevitably is lost to the surrounding, which leads to the reduction of the evaporation efficiency of the evaporator. Bae et al. [22] designs a composite membrane with light absorptivity of 91%, but the light-absorbing membrane is directly in contact with water during evaporation, resulting in an evaporation efficiency of less than 50% at a solar irradiation intensity of $1 \text{ kW}\cdot\text{m}^{-2}$. Thus, the issue of heat conduction loss from the evaporation surface to the water should be considered. Li et al. [23] prepares a graphene oxide composite film to achieve 80%

evaporation efficiency at a solar irradiation intensity of $1 \text{ kW}\cdot\text{m}^{-2}$ through a closed two-dimensional water supply channel. Wang et al. [24] adopts a cone-structured evaporator obtained by paper folding, which not only improves the absorption of the incident light but also uses a small area of water supply at the base of the vertebrae and achieves an evaporation efficiency of 83.9% at a solar irradiation intensity of $1 \text{ kW}\cdot\text{m}^{-2}$. Thus, in the case of ensuring sufficient water supply, reducing the contact area of the pores directly with the water is possible to improve the evaporation efficiency of the evaporator.

In this paper, we try to embed carbon nanotubes (CNTs), a light absorbing material, into the polyvinyl alcohol (PVA) hydrogel material, and adhere them to the surface of cellulose sponge (CS) skeleton to form the composite surface needed for solar energy interface evaporation. It not only improves the bonding strength of the light absorbing material, but also maintains the porosity of the evaporator, eliminating the complicated pore forming process of the hydrogel material. Then this paper conducts the solar interfacial evaporation experiments of the evaporator at a solar irradiation intensity of $1 \text{ kW}\cdot\text{m}^{-2}$ and analyzes the effects of carbon nanotubes concentration, polyvinyl alcohol concentration on the evaporation performance. Finally, this paper tries to optimize the contact area between the porous sponge and the water, reduce the heat loss of the evaporator to a greater extent and make more heat used for evaporation on the premise of ensuring sufficient water supply on the evaporation surface.

2. Materials and methods

2.1. Evaporators preparation

To analyze the effect of thin polyvinyl alcohol hydrogel layers on the evaporation process at the solar interface, two types of evaporators were prepared in this paper: one type of evaporator with carbon nanotubes physically bonded to the surface of the cellulose sponge skeleton was named as CS-CNTs evaporator, another type of evaporator with polyvinyl alcohol wrapped carbon nanotubes and adhered to the surface of the cellulose sponge skeleton was named as CS-CNTs-PVA evaporator.

The materials required for the preparation were as follows: (1) The multi-walled carbon nanotubes ($0.1437 \text{ g}\cdot\text{g}^{-1}$ from Suzhou Tanfeng Graphene Technology Co., Ltd., Jiangsu, China) with an outer diameter of 20–40 nm and a length of 10–30 μm . (2) Cellulose sponge ($0.0028 \text{ g}\cdot\text{cm}^{-3}$ from Dongguan Yueyang Sponge Products Co., Ltd., Guangdong, China) as water supply material, its thermal conductivity was measured by a thermal conductivity meter (Hot Disk TPS 2500S, Sweden) as $0.0527 \text{ W}\cdot\text{m}^{-1}\cdot\text{K}^{-1}$. (3) Polyvinyl alcohol powder ($0.0241 \text{ g}\cdot\text{g}^{-1}$ from Saan Chemical Technology (Shanghai) Co., Ltd., China) with a molecular mass of 15,000. (4) Glutaraldehyde cross-linking agent ($0.0146 \text{ g}\cdot\text{mL}^{-1}$ from Shanghai Maclean Biochemical Technology Co., Ltd., China), mass fraction 50%.

2.1.1. CS-CNTs evaporators preparation

Carbon nanotubes were deposited on the surface of the cellulose sponge skeleton by physical liquid-phase

deposition as shown in Fig. 1a. Firstly, CNTs of different masses (0.05, 0.1, 0.15, 0.2, 0.25, 0.3 and 0.35 g) were uniformly dispersed in 10 mL deionized water by 10 min ultrasonic dispersion to obtain seven stable suspensions of CNTs with different concentrations (5, 10, 15, 20, 25, 30 and 35 g·L⁻¹). The suspension was poured into a petri dish with a diameter of 6 cm, followed by adsorption of one face (4 cm × 4 cm) of CS (volume 4 cm × 4 cm × 4.5 cm) immersed in the petri dish for 3 min. Finally, the obtained evaporator was dried in the drying oven at 40°C for 5 h to obtain the CS-CNTs evaporator.

2.1.2. CS-CNTs-PVA evaporators preparation

In-situ polymerization was used to form thin hydrogel layers of polyvinyl alcohol wrapped carbon nanotubes on the surface of cellulose sponge skeleton, as shown in Fig. 1b. Firstly, prepared 100 mL of each PVA solution with different mass fractions (5%, 7.5%, 10%, and 12.5%), corresponding added to (625, 938, 1,250 and 1,563 μL) 50% mass fraction of glutaraldehyde cross-linking ultrasonic processing for 5 min to obtain solution A. Then, a certain mass of CNTs (0.15 and 0.35 g) and dilute hydrochloric acid (1 mL and 1.2 mol·L⁻¹) was added to 9 mL of solution A. After ultrasonic dispersion for 5 min, obtained corresponding CNTs concentrations of 15 and 35 g·L⁻¹ with PVA concentrations of 5%, 7.5%, 10% and 12.5%, respectively, total eight different combinations of solution B. Then solution B was poured into a petri dish with a diameter of 6 cm, and subsequently, one surface (4 cm × 4 cm) of CS (volume 4 cm × 4 cm × 4.5 cm) was immersed in the petri dish adsorbed for 3 min and then

removed. After PVA gelation in the surface layer of CS for 3 h, the black surface was inverted and soaked in deionized water for 5 h to remove unreacted material. Finally, the obtained evaporator was put into the drying oven at 40°C for 5 h, then the evaporator was put into deionized water to fully absorb water for 5 h, and the drying and absorbing operation was repeated 3 times.

2.2. Evaporators characterization

The porosity of the material was measured by the drainage method. First, the dry and regular shaped material was placed on the electronic balance to get the initial mass m_1 . Second, it was put into the deionized water to absorb moisture fully. Third, it was weighed the mass m_2 and calculated the volume as V in the water-filled state. The porosity ϕ of the material could be calculated by Eq. (1). The porosity ϕ_0 of the cellulose sponge was calculated at about 86.8%.

$$\phi = \frac{(m_2 - m_1)}{(\rho_w \cdot V)} \quad (1)$$

Fig. 2a shows the physical picture of the CS-CNTs-PVA evaporator with a length of 40 mm, a width of 40 mm and a height of 45 mm. Fig. 2b shows the surface of cellulose sponge, the PVA powder, the surface of CS-CNTs-PVA evaporator, and the surface of CS-CNTs evaporator which have been analyzed by Fourier-transform infrared spectroscopy (Thermo Scientific Nicolet iS20, United States of America), respectively. The spectrum of the cellulose sponge

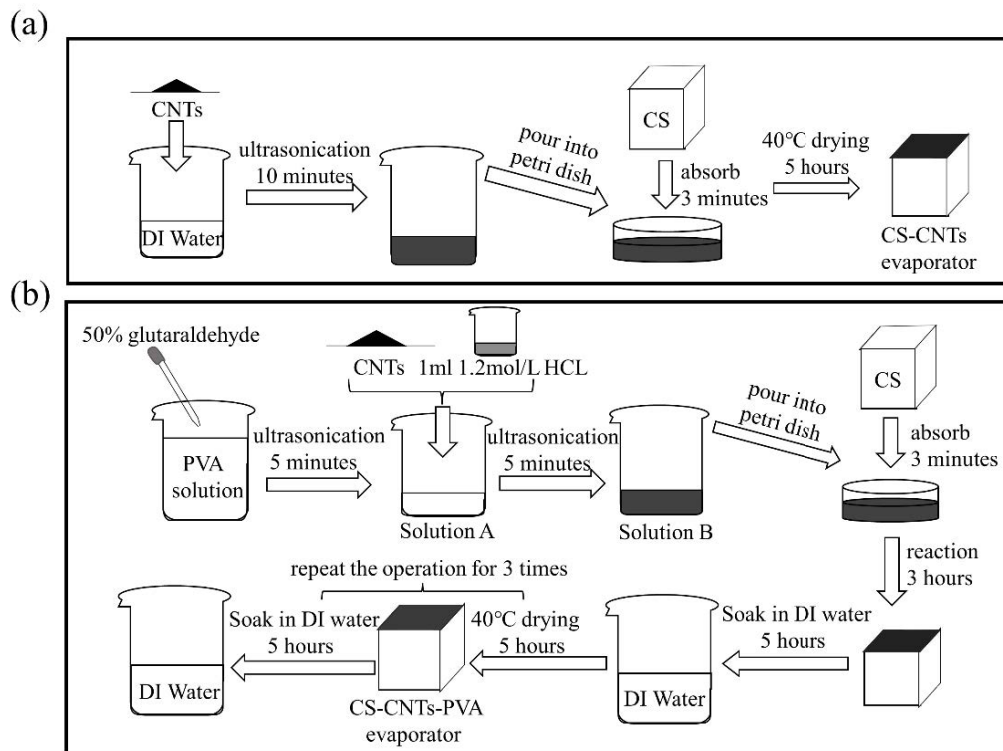


Fig. 1. Evaporators preparation: schematic diagram of (a) CS-CNTs evaporator preparation and (b) CS-CNTs-PVA evaporator preparation.

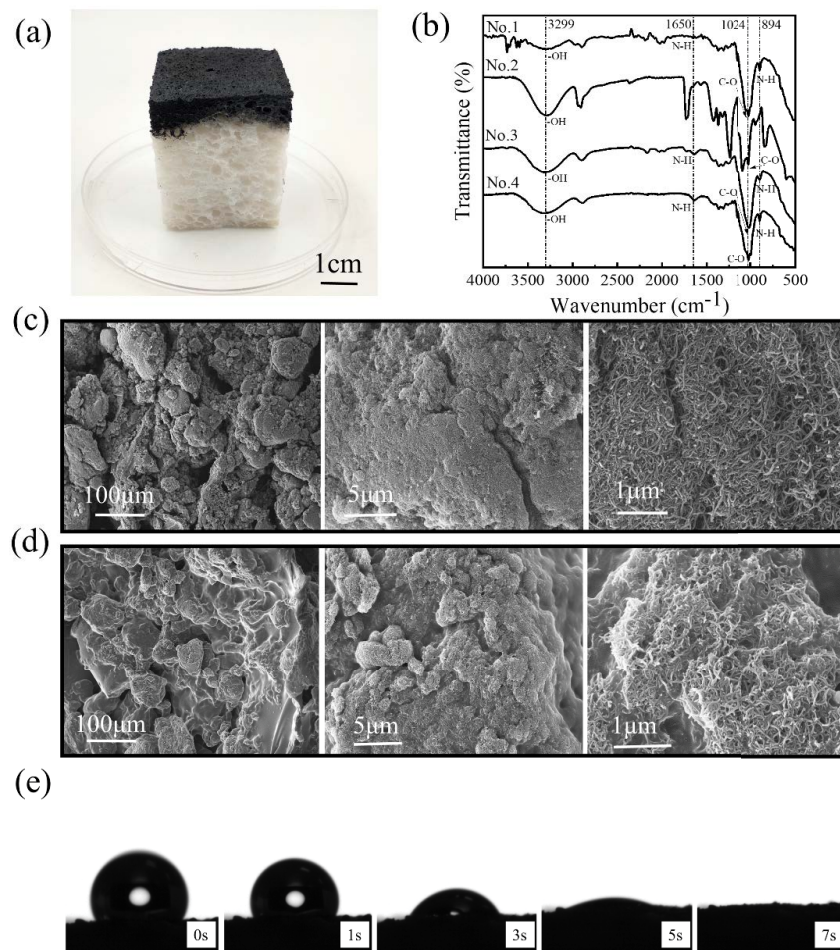


Fig. 2. Evaporators characterization: (a) physical diagram of CS-CNTs-PVA evaporator, (b) Fourier-transform infrared spectra diagram of PVA powder (No. 2), surfaces of cellulose sponge (No. 1), CS-CNTs-PVA evaporator (No. 3), and CS-CNTs evaporator (No. 4), (c) scanning electron microscopy diagram of CS-CNTs evaporator surface, (d) scanning electron microscopy diagram of CS-CNTs-PVA evaporator surface and (e) change of contact angle of composite surface.

(No. 1 in Fig. 2b) shows that $-OH$ and $C-O$ telescopic vibration are observed at $3,299$ and $1,024$ cm^{-1} , respectively, and the peak at 894 and $1,650$ cm^{-1} are attributed to $N-H$ bending vibration. In the PVA spectrum (No. 2 in Fig. 2b), the peaks at $3,286$ and $1,022$ cm^{-1} are attributed to $-OH$ and $C-O$ telescopic vibration, respectively. All characteristic peaks of CS and PVA were found in the spectra of the CS-CNTs-PVA evaporator (No. 3 in Fig. 2b) and CS-CNTs evaporator (No. 4 in Fig. 2b) without shifts, further indicating the presence of the above substances in the evaporation surface. Fig. 2c shows the scanning electron microscopy (SEM) images of the evaporation surface of CS-CNTs evaporator with CNTs concentration of 15 $g \cdot L^{-1}$ taken with a scanning electron microscope (TESCAN MIRA LMS, Czech Republic). The pores can transport water by capillary force to the evaporation surface. Increasing magnification reveals that the CNTs are visible and evenly distributed on the surface of cellulose sponge skeleton. Thus, the sunlight is directly absorbed by the CNTs of the surface and heats the surface water. Fig. 2d shows SEM images taken of the evaporation surface of CS-CNTs-PVA evaporator with CNTs concentration of 15 $g \cdot L^{-1}$ modified with a mass fraction of

10% PVA. The cover showed pores with diameters of about 80 – 150 μm wide. Increasing magnification, the micron channels formed by carbon nanotubes and polyvinyl alcohol hydrogel could be seen. The overall water transport of the CS-CNTs-PVA evaporator was supported by the internal pores of the cellulose sponge skeleton and the rapid water diffusion near the evaporation surface was assisted by the nanochannels. Fig. 2e shows the contact angle of the composite surface measured with the contact angle measuring instrument (Kruss DSA 25, Germany). The water can wet the carbon nanotube polyvinyl alcohol composite surface easily. It indicates that the surface pore structure has strong capillary force, which is conducive to the rapid diffusion of water.

2.3. Solar interfacial evaporation experiment

2.3.1. Experimental equipment and procedures

Fig. 3 shows the schematic diagram of the evaporation experiment. The leading equipment includes a solar simulator (Solar-500, Beijing Newbit Technology Co., Ltd.,

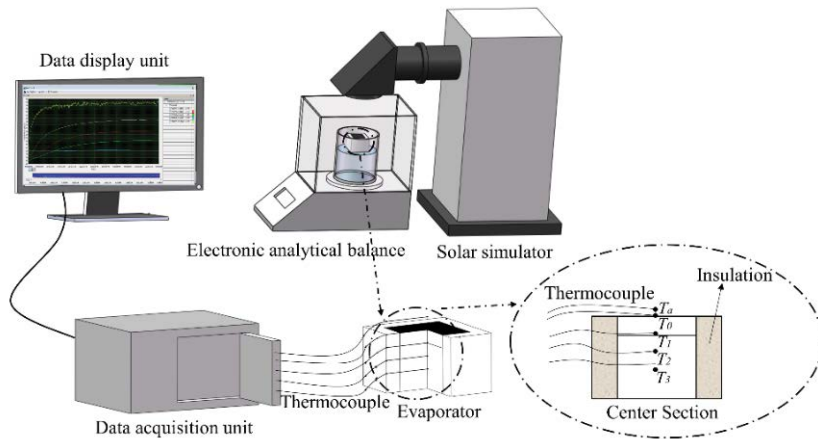


Fig. 3. Schematic diagram of evaporation experiment.

China) for simulating sunlight, an irradiation meter (GEL-NP2000-2A, Beijing Zhongjiao Jinyuan Technology Co., Ltd., China), accuracy of $0.01 \text{ mW}\cdot\text{cm}^{-2}$, for measuring the intensity of sunlight irradiation, electronic analytical balance (G&G JJ1023BF, Changshu Shuangjie Testing Instrument Factory, China), accuracy of 0.001 g , for recording the mass changes during the experiment, a data acquisition unit (National Instruments, Austin, TX, USA) for measuring the real-time temperature and recording on the computer. T-type thermocouple, accuracy 0.1°C , for measuring the temperature of the evaporation surface T_{ev} , the temperature of the environment at 2 mm above evaporation surface T_a , the temperature at 10 mm interval inside the evaporators as T_1 , T_2 , T_3 , temperature measurement points as shown in Fig. 3.

Solar interfacial evaporation was performed in experiments at room temperature of 25°C and ambient relative humidity of 60% . The solar irradiation intensity of composite surfaces is $1 \text{ kW}\cdot\text{m}^{-2}$ because of the daily maximum solar irradiation is about $1 \text{ kW}\cdot\text{m}^{-2}$. The experimental steps were as follows: (1) the solar simulator was turned on, and adjusted the irradiation intensity of the light source to $1 \text{ kW}\cdot\text{m}^{-2}$ using an irradiation meter. (2) The evaporator was surrounded using a 2 cm thick polyethylene foam for insulation. (3) Placed the thermocouples on the temperature measurement points of the evaporator and put the evaporator into the beaker with 200 mL , 25°C deionized water. (4) Placed the beaker on the electronic analytical balance under the light source. The thermocouples signal was collected in real-time during the experiment using a data acquisition instrument, and the beaker quality changes was recorded by an electronic analytical balance every 5 min interval.

2.3.2. Experimental data processing and error analysis

To effectively assess the water evaporation performance of the evaporator, the evaporation rate and efficiency of the evaporator evaporation process should be calculated. Eq. (2) is the evaporation rate w of the evaporator, which is used to characterize the mass of water evaporation per unit of time and area.

$$w = \frac{m}{(s \cdot t)} \quad (2)$$

Eq. (3) defines the evaporation efficiency η_{evap} as the proportion of water used for evaporation under incident energy. $h_{L,V}$ is the enthalpy of water evaporation, calculated using Eq. (4), where C_p is the constant pressure heat capacity of water, taken as $4.2 \text{ kJ}\cdot\text{kg}^{-1}\cdot^\circ\text{C}^{-1}$, ΔT is the evaporation surface temperature difference at initial and the steady state during the experiment, $h_{L,G}$ is latent heat of water at interface temperature, calculated using Eq. (5) [25].

$$\eta_{\text{evap}} = \frac{q_{\text{evp}}}{I} = \frac{w \cdot h_{L,V}}{I} \quad (3)$$

$$h_{L,V} = h_{L,G} + C_p \cdot \Delta T \quad (4)$$

$$h_{L,G} = 1.91846 \times 10^6 \left[\frac{T}{(T - 33.91)} \right]^2 \quad (5)$$

The relative error of evaporation rate δ_w/w in the measurement process is calculated by Eq. (6), where δ_m , δ_{A_2} and δ_t are the maximum measurement errors of evaporated mass, evaporation area, and experiment time, respectively, where m , A_2 , and t correspond to the evaporated mass, evaporation area, and experiment time, respectively. The relative error of evaporation efficiency $\delta\eta/\eta$ is calculated by Eq. (7), where δ_I is the light intensity measurement error.

$$\frac{\delta_w}{w} = \sqrt{\frac{2\delta_m^2}{m^2} + \frac{\delta_{A_2}^2}{A_2^2} + 2\frac{\delta_t^2}{t^2}} \quad (6)$$

$$\frac{\delta_\eta}{\eta} = \sqrt{\frac{\delta_w^2}{w^2} + \frac{\delta_I^2}{I^2}} \quad (7)$$

In the whole experiment, the minimum mass loss of evaporation m was 0.665 g , which was measured by an electronic analytical balance with an uncertainty δ_m of $\pm 0.001 \text{ g}$, the surface area uncertainty δ_{A_2} was $\pm 0.4 \text{ cm}^2$ which calculated from the ruler error of 0.5 mm , and A_2 was 16 cm^2 , the experiment time uncertainty δ_t was $\pm 1 \text{ s}$, and t was $3,600 \text{ s}$. Bringing into Eq. (6) got the maximum relative error of evaporation rate as 2.51% . The irradiation meter

uncertainty δ , was $\pm 0.01 \text{ mW}\cdot\text{cm}^{-2}$, and I corresponded to the incident light intensity of $100 \text{ mW}\cdot\text{cm}^{-2}$. Bringing into Eq. (7) got the maximum relative error of evaporation efficiency as 2.51%.

2.3.3. Energy distribution analysis of evaporation process

Fig. 4 shows the energy distribution of the evaporation process. The energy shares of each component η_{rad} , η_{conv} , η_{cond} , and η_{ref} are the ratio of each component's energy to the total incident energy, respectively. Eq. (8) is the energy conservation equation of the evaporation surface.

$$I = q_{\text{evap}} + q_{\text{rad}} + q_{\text{conv}} + q_{\text{cond}} + q_{\text{ref}} \quad (8)$$

Eq. (9) for calculating the radiation heat loss of the evaporation surface to the upper air, where σ is Stefan–Boltzmann constant, its value is $5.67 \times 10^{-8} \text{ W}\cdot\text{m}^{-2}\cdot\text{C}^{-4}$, ε is the evaporation surface emissivity, taking the value of light absorptivity α of the evaporation surface. The evaporation surface was surrounded by the heated steam in the experiment, and the temperature of the environment near the evaporation surface was very close to the temperature of the evaporation surface, so the thermocouple was usually placed near the top of the evaporation surface [26]. Here T_a was obtained by measuring the temperature at 2 mm above the evaporation surface.

$$q_{\text{rad}} = \varepsilon \cdot \sigma \cdot (T_0^4 - T_a^4) \quad (9)$$

Eq. (10) for calculating heat convection loss of evaporation surface to the upper air, where h is the convection heat transfer coefficient of evaporation surface, take value of $6 \text{ W}\cdot\text{m}^{-2}\cdot\text{C}^{-1}$.

$$q_{\text{conv}} = h \cdot (T_0 - T_a) \quad (10)$$

Eq. (11) for calculating heat conduction loss from the evaporation surface to the water [27], the evaporator can be considered a one-dimensional steady state thermal

conductivity under good adiabatic conditions. λ is the composite thermal conductivity in the water-filled state of the water supply layer, which is calculated based on the material porosity and composition in Eq. (12). The composite thermal conductivity of the cellulose sponge in a water-filled state was about $0.528 \text{ W}\cdot\text{m}^{-1}\cdot\text{C}^{-1}$.

$$q_{\text{cond}} = \left(\frac{A_1}{A_2} \right) \cdot \lambda \cdot \left(\frac{\Delta T}{\Delta L} \right) \quad (11)$$

$$\lambda = \phi \cdot \lambda_w + (1 - \phi) \cdot \lambda_c \quad (12)$$

Eq. (13) for calculating the reflection heat loss of the incident energy on the evaporation surface, where ρ is light reflectance.

$$q_{\text{ref}} = \rho \cdot I \quad (13)$$

3. Results and discussion

3.1. Interfacial evaporation characteristics of CS-CNTs evaporator

This paper prepared CS-CNTs evaporators with different carbon nanotubes concentrations (5, 10, 15, 20, 25, 30, and 35 $\text{g}\cdot\text{L}^{-1}$) and analyzed the effect of carbon nanotubes content on the interfacial evaporation of CS-CNTs evaporator. Fig. 5a shows the results of the evaporation experiments. With the increase of CNTs concentration, the evaporation rate gradually increased and then tended to be flat. When the concentration of CNTs increased to 15 $\text{g}\cdot\text{L}^{-1}$, the evaporation rate of the evaporator was $1.107 \text{ kg}\cdot\text{m}^{-2}\cdot\text{h}^{-1}$, and the evaporation efficiency reached 73.2%, which was slightly lower than the CNTs concentration of 35 $\text{g}\cdot\text{L}^{-1}$ with evaporation rate $1.120 \text{ kg}\cdot\text{m}^{-2}\cdot\text{h}^{-1}$ and evaporation efficiency 74.1%.

The spectra reflectance (ρ) and transmittance (t) were measured by the UV-Vis-NIR spectrophotometer (UV-3600i Plus, Shimadzu, Japan), and the light absorptivity was calculated by $\alpha = 1 - \rho - t$. Fig. 5b shows the light absorptivity of the evaporation surface of CS-CNTs evaporator with CNTs concentrations of 0, 15, and 35 $\text{g}\cdot\text{L}^{-1}$. The light absorptivity for CNTs concentrations of 15 and 35 $\text{g}\cdot\text{L}^{-1}$ was 97.4% and 97.5%, respectively, much higher than the evaporator without CNTs (14.1%).

Fig. 5c shows the temperature (T_0 , T_1 , T_2 , T_3) difference during the experiment of CS-CNTs evaporator with CNTs concentrations of 15 and 35 $\text{g}\cdot\text{L}^{-1}$. For the CS-CNTs evaporators with CNTs concentrations of 15 and 35 $\text{g}\cdot\text{L}^{-1}$, the temperature measurement results as the evaporator reached a steady state, and the five primary energy distribution ratios are shown in Table 1 (category (1) and (2), respectively). The leading energy of the system was used by water evaporation, but the heat conduction loss accounts for the largest proportion of the four energy losses. Though the cellulose sponge had a low thermal conductivity and played a role in isolating the evaporation surface from the water, the thermal conductivity of the cellulose sponge in a water-filled state was 88% of the thermal conductivity of the water at the same temperature state, resulting in its heat conduction loss to the water was still prominent.

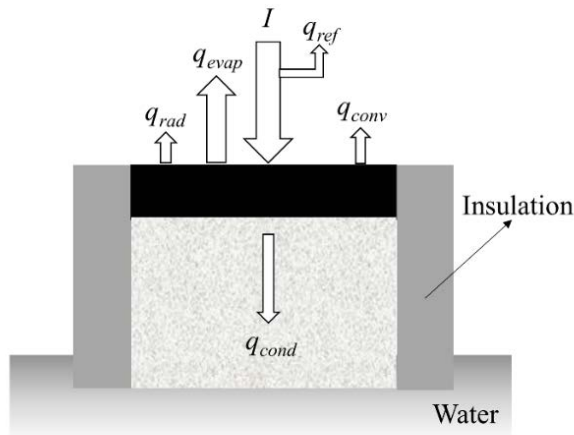


Fig. 4. Schematic diagram of evaporation process energy distribution.

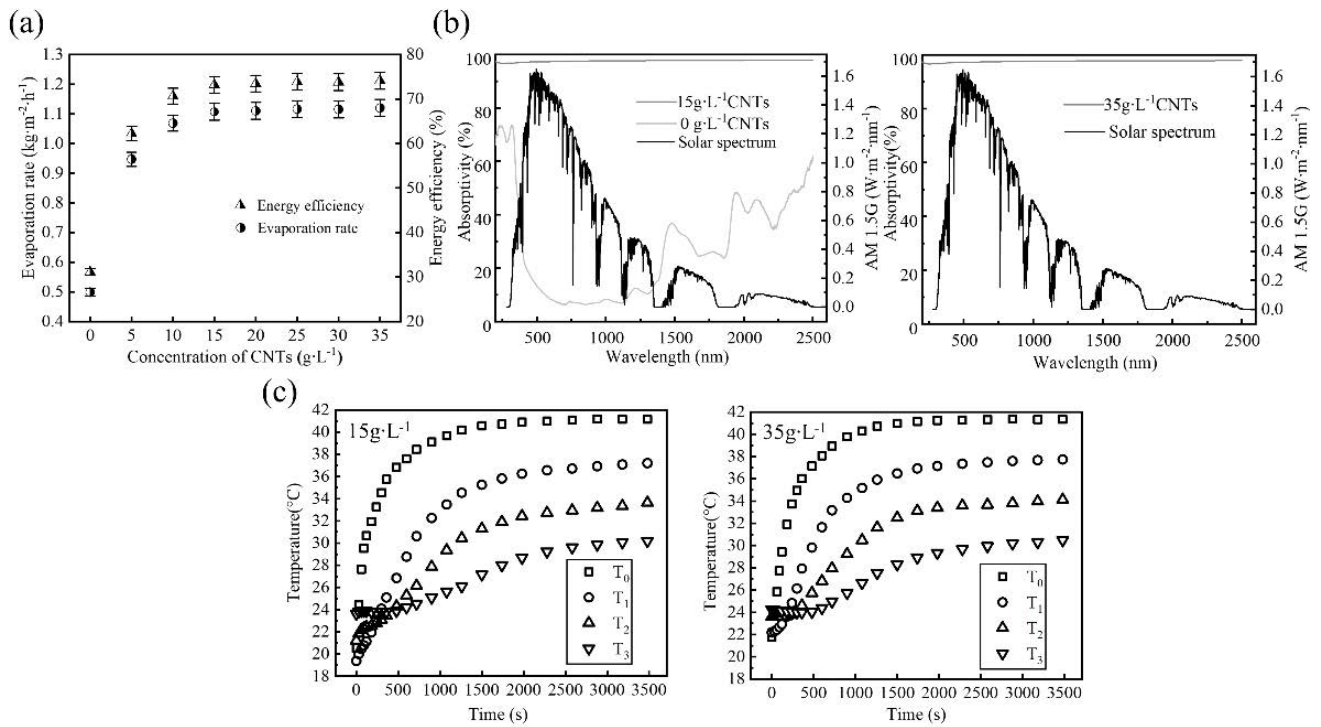


Fig. 5. Interfacial evaporation properties of CS-CNTs evaporator: (a) evaporation rate and efficiency of CS-CNTs evaporators with different CNTs concentrations, (b) UV-Vis-NIR spectra diagram of CS-CNTs evaporation surfaces with CNTs concentrations of 0, 15 and 35 g·L⁻¹ and (c) temperature (T_0 , T_1 , T_2 , T_3) difference of CS-CNTs evaporators with CNTs concentrations of 15 and 35 g·L⁻¹.

Table 1
Temperature measurement results and five primary energy distribution ratios of different evaporators at a steady state

Category	T_0 (°C)	T_u (°C)	$\Delta T/\Delta L$ (°C·m ⁻¹)	η_{conv} (%)	η_{cond} (%)	η_{rad} (%)	η_{ref} (%)	η_{evap} (%)
(1)	41.1	38.1	364	1.8	19.2	2.0	2.6	73.2
(2)	41.3	38.4	360	1.7	19.0	2.0	2.5	74.1
(3)	41.8	39.1	310	1.6	16.4	1.8	2.6	78.2
(4)	42.7	39.9	315	1.7	3.3	1.9	2.6	89.7

3.2. Interfacial evaporation properties of CS-CNTs-PVA evaporator modified with polyvinyl alcohol

This paper chemically modified the evaporation surface of CS-CNTs evaporator by introducing transparent and hydrophilic PVA and called it a modified layer. To investigate the effect of PVA content on the interfacial evaporation properties of CS-CNTs-PVA evaporator, CS-CNTs-PVA evaporators with different PVA mass fractions (5%, 7.5%, 10%, and 12.5%) based on the CNTs concentration of 15 and 35 g·L⁻¹ were prepared.

Fig. 6a shows the interfacial evaporation properties of CS-CNTs-PVA evaporator with different PVA concentrations. The CNTs concentrations of 15 and 35 g·L⁻¹ showed similar patterns at different PVA concentrations. With the increase of PVA concentration, the evaporation rate was further increased relative to the evaporation surface before modification, and it reached the extreme value at a concentration

of about 10%. The UV-Vis-NIR spectra in Fig. 6b shows the light absorptivity of evaporation surface with CNTs concentrations 15 and 35 g·L⁻¹ modified with 10% PVA, which are still presenting 97.4% and 97.5% light absorptance in the whole solar spectrum, respectively, indicating that the transparent polyvinyl alcohol did not affect the light absorptivity of the CNTs. Based on the similarity of their light absorptivity and evaporation rate, from the perspective of material saving, the following analyses are for evaporator with CNTs concentration of 15 g·L⁻¹ modified with 10% PVA.

Fig. 6c shows the porosity of the modified layer using the drainage method and density in a water-filled state of the modified layer for CNTs concentration of 15 g·L⁻¹ with different PVA concentrations. Its porosity and density gradually decreased with the increase of PVA concentration. When the PVA concentration reached 12.5%, the evaporation surface presented localized dryness in the process of the experiment due to the decrease of porosity.

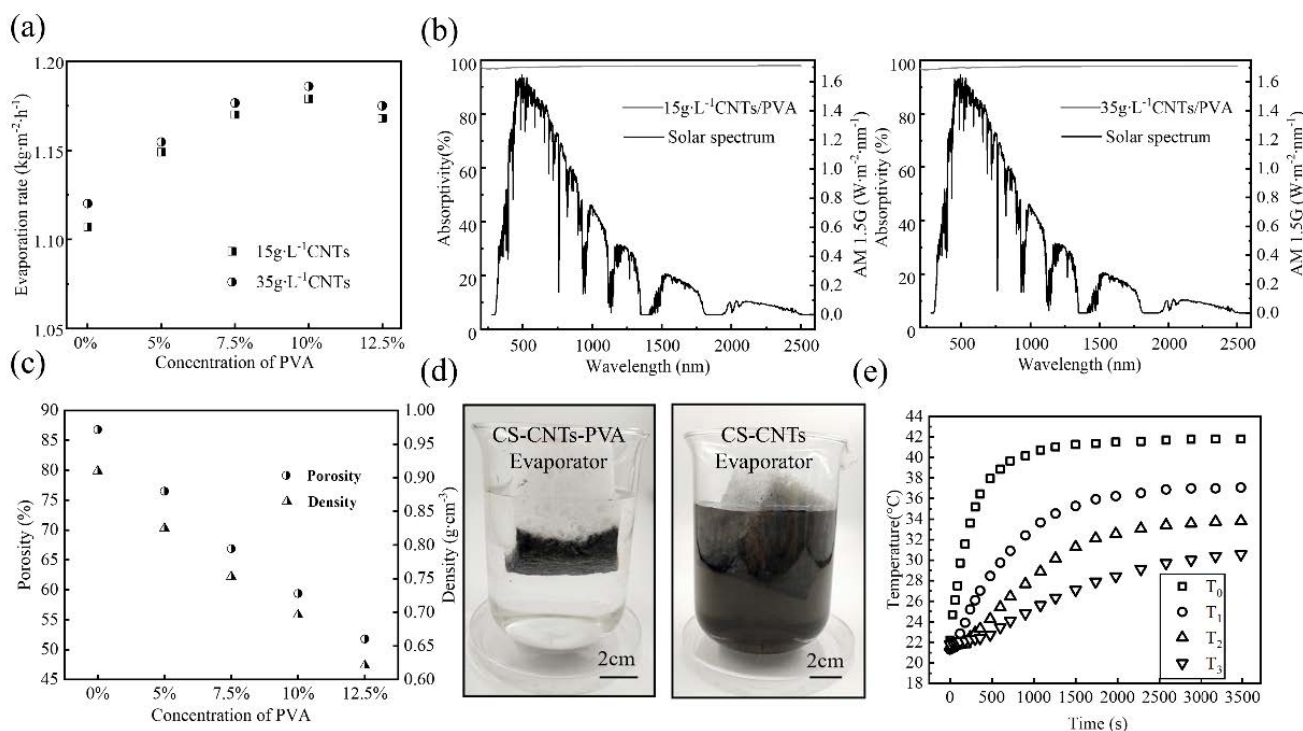


Fig. 6. Interfacial evaporation properties of CS-CNTs-PVA evaporator modified with polyvinyl alcohol: (a) evaporation rate changes of CS-CNTs-PVA evaporators of CNTs concentrations of 15 and 35 g·L⁻¹ modified with different concentrations of PVA, (b) UV-Vis-NIR spectra diagram of evaporation surfaces with CNTs concentrations of 15 and 35 g·L⁻¹ modified with 10% PVA, (c) porosity and density in water-filled state changes of modified layer with different PVA concentrations in CNTs concentrations of 15 g·L⁻¹, (d) comparison of interface stability of CS-CNTs evaporator and CS-CNTs-PVA evaporator of CNTs concentration of 15 g·L⁻¹ and (e) temperature variation at 10 mm interval inside CS-CNTs-PVA evaporator of CNTs concentration 15 g·L⁻¹ modified with 10% PVA.

Fig. 6d shows the interfacial stability of evaporators with CNTs concentration of 15 g·L⁻¹ was compared before and after 10% PVA modified in deionized water after extrusion and stirring by external force. For the CS-CNTs evaporator, the CNTs fell off and water become turbid, because of the carbon nanotubes physically adhered to the sponge skeleton surface, and the binding strength was weak. In contrast, the CS-CNTs-PVA evaporator, the water was still clear, for the thin hydrogel layer formed by PVA hydrogel wrapped CNTs could firmly adhere to the surface of the sponge skeleton, the modified layer retained the elasticity and porous of the original sponge and enhanced the binding strength of CNTs to the evaporation surface.

For the CS-CNTs-PVA evaporator with CNTs concentration of 15 g·L⁻¹ modified with 10% PVA, its evaporation rate increased by 0.072 kg·m⁻²·h⁻¹ compared to without PVA modified, and the porosity of the modified layer decreased to 59.4%. The modified layer thermal conductivity in a dry state was measured by thermal conductivity meter as 0.0684 W·m⁻¹·°C⁻¹, so the modified layer composite thermal conductivity in the water-filled state was calculated to be about 0.379 W·m⁻¹·°C⁻¹ in Eq. (12), which was 28.2% lower than that before modified (0.528 W·m⁻¹·°C⁻¹), which also explained that the evaporation efficiency of the evaporator increases when the PVA concentration increases.

For the CS-CNTs-PVA evaporator with CNTs concentration of 15 g·L⁻¹ modified with 10% PVA, Fig. 6e shows the

temperature variation at 10 mm interval inside CS-CNTs-PVA evaporator. Compared to the temperature gradient of the modified layer (460°C·m⁻¹) was 32.6% higher than that of the water supply layer (310°C·m⁻¹), which also confirmed the overall reduced thermal conductivity of the modified layer. The temperature measurement results as the evaporator reached a steady state, and the five primary energy distribution ratios are shown in Table 1 (category 3), in which heat conduction loss was still the most significant factor affecting the evaporation efficiency.

3.3. Interfacial evaporation characteristics of CS-CNTs-PVA evaporator after optimization the area of water supply path

According to the above study, for the CS-CNTs-PVA evaporator with CNTs concentration of 15 g·L⁻¹ modified with 10% PVA, there was still about 16.4% of the heat lost in heat conduction. To reduce this energy loss, this paper optimized the water supply path by reducing the area of the water supply path and replacing it with the polyethylene foam.

Fig. 7a shows the water supply path area was reduced in the CS-CNTs-PVA evaporator with CNTs concentration of 15 g·L⁻¹ modified with 10% PVA, the ratio of the water path area was recorded as A_1/A_2 . Fig. 7b shows the evaporation rates and evaporation efficiencies under different ratios of water supply path area. The results showed that

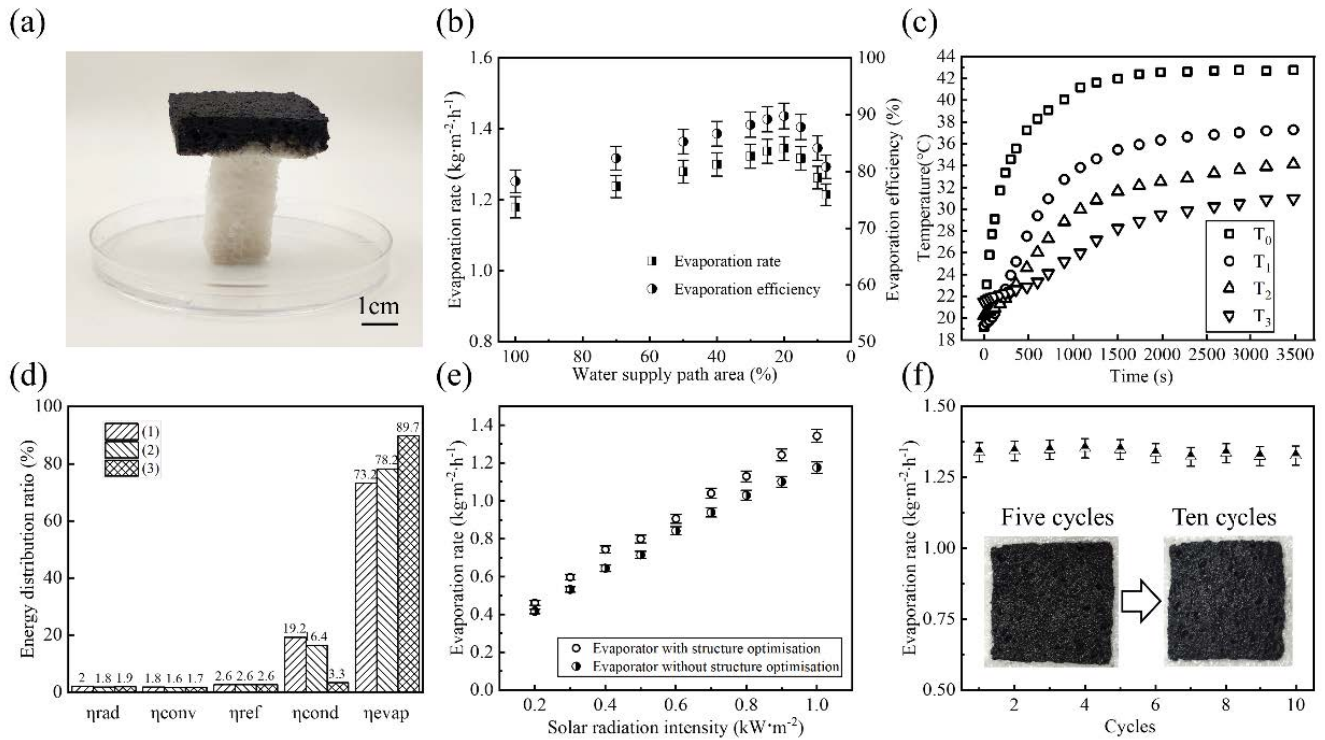


Fig. 7. Interfacial evaporation properties of CS-CNTs-PVA evaporator with CNTs concentration of $15 \text{ g}\cdot\text{L}^{-1}$ modified with 10% PVA after optimization area ratio of water supply path: (a) physical diagram of CS-CNTs-PVA evaporator after optimization, (b) evaporation rate and efficiency changes of CS-CNTs-PVA evaporator under different ratios of water supply path area, (c) under optimal ratio of water supply path area of 20%, temperature variation at 10 mm interval inside of CS-CNTs-PVA evaporator, (d) energy distribution diagram of CS-CNTs evaporator of CNTs concentration $15 \text{ g}\cdot\text{L}^{-1}$, CS-CNTs-PVA evaporator and CS-CNTs-PVA evaporator with ratio of water supply path area of 20%. (e) Evaporation performance of CS-CNTs-PVA evaporators with 100% and 20% of water supply path area ratio as a function of solar irradiation intensity. (f) Evaporation performance of CS-CNTs-PVA evaporator with ratio of water supply path area of 20% for 10 cycles of testing.

the evaporation rate and evaporation efficiency increased gradually with the reduction of the water supply path area, and the evaporation rate reached an extreme value when the ratio of water supply path area was about 20%, the evaporation rate of the evaporator was $1.345 \pm 0.034 \text{ kg}\cdot\text{m}^{-2}\cdot\text{h}^{-1}$ with an evaporation efficiency of $89.7\% \pm 2.5\%$ at this time. Then the evaporation rate slightly reduced due to the surface localized insufficient water supply.

For the CS-CNTs-PVA evaporator with the ratio of water supply path area of 20%, the temperature variation at 10 mm interval inside CS-CNTs-PVA evaporator is shown in Fig. 7c. The temperature measurement results as the evaporator reached a steady state and the five primary energy distribution ratios are shown in Table 1 (category 4). Fig. 7d is the energy distribution diagram of evaporators. (1)–(3) in the legend represent the energy distribution of the CS-CNTs evaporator, the CS-CNTs-PVA evaporator and the CS-CNTs-PVA evaporator with the ratio of water supply path area of 20%, respectively. The evaporation efficiency improved by 16.5% compared to the initial CS-CNTs evaporator without optimizing water supply path area.

Since the solar irradiation intensity varies throughout the day, approaching $1 \text{ kW}\cdot\text{m}^{-2}$ around midday on a clear day, it is necessary to investigate the effect of solar irradiation intensity on evaporation performance. Adjusting the solar irradiation intensity variation range of $0.2\text{--}1.0 \text{ kW}\cdot\text{m}^{-2}$

in $0.1 \text{ kW}\cdot\text{m}^{-2}$ increments, the CS-CNTs-PVA evaporators with 100% and 20% of the water supply path area ratio were experimented sequentially, and the results are shown in Fig. 7e. The results showed that the evaporation performance of the evaporator after water supply path area optimization was higher than that before optimization under different solar irradiation intensities, and the evaporation rate of the two evaporators increased linearly with the increase of solar irradiation intensity.

As shown in Fig. 7f, the cyclability of the CS-CNTs-PVA evaporator with the ratio of water supply path area of 20% was experimentally analyzed in this paper to understand the durability of its use. The results showed that the evaporator was intact and maintained an average evaporation rate of $1.337 \text{ kg}\cdot\text{m}^{-2}\cdot\text{h}^{-1}$ for 10 cycles (120 min for one cycle, fully submerged in water when not experimented) at a solar irradiation intensity of $1 \text{ kW}\cdot\text{m}^{-2}$, with a maximum fluctuation of 1.6% from the initial evaporation rate.

4. Conclusion

This paper proposes a composite surface by wrapping carbon nanotubes on the surface of cellulose sponge skeleton using polyvinyl alcohol hydrogel and analyzes the effects of carbon nanotubes concentration, polyvinyl alcohol concentration, and water supply path area on the

performance of the evaporator. The research leads to the following conclusions:

- The concentration of carbon nanotubes affects the light absorptivity and evaporation efficiency of the evaporator. When the concentration of carbon nanotubes reaches 15 g·L⁻¹, the light absorptivity of the surface reaches 97.4%. The light absorptivity and evaporation efficiency does not increase more when the concentration of carbon nanotubes continue to grow.
- With the introduction of polyvinyl alcohol on the evaporation surface, the carbon nanotubes are more firmly bound to the surface of the cellulose sponge skeleton, and the light absorptivity of the evaporation surface is not reduced. For the evaporation surface modified with the polyvinyl alcohol hydrogel, its evaporation efficiency reaches maximum when the concentration of polyvinyl alcohol is about 10%.
- Heat conduction loss from the evaporation surface to the water is the most considerable energy loss in solar interfacial evaporation. Reducing the water supply path area of the evaporator and replacing it with the heat insulation polyethylene foam can improve the evaporation efficiency. Under the optimal ratio of the water supply path area of 20%, at a solar irradiation intensity of 1 kW·m⁻², the evaporation rate of the evaporator reaches 1.345 ± 0.034 kg·m⁻²·h⁻¹ with an evaporation efficiency of 89.7% ± 2.5%, the evaporation rate increased linearly with the increase of solar irradiation intensity, and evaporator evaporation performance with a long-term stability.

Declaration of interests

All of the authors declare no competing financial interests.

Data availability

The data that support the findings of this research are openly available at Mendeley Data. Wang, yifan; Su, Fengmin; Fan, Yiming; Ji, Yulong; Zhao, Nannan (2022), "Solar Interfacial Evaporation Properties of Carbon Nanotube Polyvinyl Alcohol Composite Surface", Mendeley Data, V1, Doi: 10.17632/3pr7m8wpt.1.

Credit authorship contribution statement

Yifan Wang: Formal analysis, Data curation, Writing – original draft. Fengmin Su: Conceptualization, Methodology, Writing – review & editing, Supervision. Yiming Fan: Investigation, Writing – review & editing. Yulong Ji: Investigation, Writing – review & editing. Nannan Zhao: Investigation, Writing – review & editing.

Acknowledgements

The work presented in this article was supported by the National Natural Science Foundation of China (Contract No. 51906028) and the Applied Basic Research Program Project of Liaoning Province (Contract No. 2023JH2/101300152).

Symbols

A_1	—	Water supply path area, m ²
A_2	—	Evaporation surface area, m ²
C_p	—	Constant pressure heat capacity of water, kJ·kg ⁻¹ ·°C ⁻¹
h_{Lv}	—	Enthalpy of water evaporation, kJ·kg ⁻¹
h_{Lg}	—	Latent heat of water, kJ·kg ⁻¹
h	—	Heat convection coefficient of evaporation surface, W·m ⁻² ·°C ⁻¹
I	—	Incident energy, kW·m ⁻²
m	—	Mass loss of evaporation, g
q_{evap}	—	Energy for evaporation, kW·m ⁻²
q_{cond}	—	Energy for heat conduction loss, kW·m ⁻²
q_{rad}	—	Energy for heat radiation loss, kW·m ⁻²
q_{conv}	—	Energy for heat convection loss, kW·m ⁻²
q_{ref}	—	Energy for light reflection heat loss, kW·m ⁻²
t	—	Time of evaporation experiment, s
T_a	—	Air temperature at 2 mm above evaporation surface, °C
T_0	—	Temperature at the evaporation surface, °C
T_1	—	Temperature at the first place inside the evaporator, °C
T_2	—	Temperature at the second place inside the evaporator, °C
T_3	—	Temperature at the third place inside the evaporator, °C
$\Delta T/\Delta L$	—	Temperature gradient of 10 mm interval inside the evaporators, °C·m ⁻¹
w	—	Evaporation rate, kg·m ⁻² ·h ⁻¹

Greek

α	—	Light absorptivity of the evaporation surface, %
ρ	—	Light reflectance of the evaporation surface, %
η_{evap}	—	Evaporation efficiency, %
η_{cond}	—	Ratio of energy for heat conduction loss to the incident energy, %
η_{rad}	—	Ratio of energy for heat radiation loss to the incident energy, %
η_{conv}	—	Ratio of energy for heat convection loss to the incident energy, %
η_{ref}	—	Ratio of energy for light reflection loss to the incident energy, %
λ_w	—	Thermal conductivity of water, W·m ⁻¹ ·°C ⁻¹
λ_m	—	Thermal conductivity of the material in the dry state, W·m ⁻¹ ·°C ⁻¹
ρ_w	—	Density of the water, kg·m ⁻³
ϕ	—	Material porosity, %

Subscripts

conv	—	Convection
cond	—	Conduction
evap	—	Evaporation
m	—	Material, mass
rad	—	Radiation
ref	—	Reflection
w	—	Water

References

- [1] M. Elimelech, W.A. Phillip, The future of seawater desalination: energy, technology, and the environment, *Science*, 333 (2011) 712–717.
- [2] M. Maria Antony Raj, K. Kalidasa Murugavel, T. Rajaseenivasan, K. Srithar, A review on flash evaporation desalination, *Desal. Water Treat.*, 57 (2016) 13462–13471.
- [3] J. Li, M. Du, G. Lv, L. Zhou, X. Li, L. Bertoluzzi, C. Liu, S. Zhu, J. Zhu, Interfacial solar steam generation enables fast-responsive, energy-efficient, and low-cost off-grid sterilization, *Adv. Mater.*, 30 (2018) 1805159, doi: 10.1002/adma.201805159.
- [4] J.R. Betancort Rodríguez, V. Millán Gabet, G. Melián Monroy, A. Bello Puerta, I. Fonseca Barrio, Distilled and drinkable water quality produced by solar membrane distillation technology, *Desal. Water Treat.*, 51 (2013) 1265–1271.
- [5] H. Ghasemi, G. Ni, A.M. Marconnet, J. Loomis, S. Yerci, N. Miljkovic, G. Chen, Solar steam generation by heat localization, *Nat. Commun.*, 5 (2014) 4449, doi: 10.1038/ncomms5449.
- [6] P. Tao, G. Ni, C. Song, W. Shang, J. Wu, J. Zhu, G. Chen, T. Deng, Solar-driven interfacial evaporation, *Nat. Energy*, 3 (2018) 1031–1041.
- [7] Z. Fan, J. Ren, H. Bai, P. He, L. Hao, N. Liu, B. Chen, R. Niu, J. Gong, Shape-controlled fabrication of MnO/C hybrid nanoparticle from waste polyester for solar evaporation and thermoelectricity generation, *Chem. Eng. J.*, 451 (2023) 138534, doi: 10.1016/j.cej.2022.138534.
- [8] B. Chen, J. Ren, Y. Song, P. He, H. Bai, Z. Fan, R. Niu, J. Gong, Upcycling waste poly(ethylene terephthalate) into a porous carbon cuboid through a MOF-derived carbonization strategy for interfacial solar-driven water–thermoelectricity cogeneration, *ACS Sustainable Chem. Eng.*, 10 (2022) 16427–16439.
- [9] C. Miao, J. Ren, M. Wang, C. Xie, L. Zhang, Q. Li, H. Zhang, Performance analysis of a solar seawater desalination using an ultra-black nylon flocking material, *Desal. Water Treat.*, 252 (2022) 18–27.
- [10] E.-D. Miao, M.-Q. Ye, C.-L. Guo, L. Liang, Q. Liu, Z.-H. Rao, Enhanced solar steam generation using carbon nanotube membrane distillation device with heat localization, *Appl. Therm. Eng.*, 149 (2019) 1255–1264.
- [11] V.M. Ovando-Medina, A.G. Escobar-Villanueva, H. Martínez-Gutiérrez, O. González-Ortega, Interfacial photothermal water evaporator based on nanoporous microwave-expanded graphite and coconut waste fibers@recycled polystyrene as substrate, *Int. J. Energy Res.*, 44 (2020) 10878–10893.
- [12] Y. Liu, S. Yu, R. Feng, A. Bernard, Y. Liu, Y. Zhang, H. Duan, W. Shang, P. Tao, C. Song, T. Deng, A Bioinspired, Reusable, paper-based system for high-performance large-scale evaporation, *Adv. Mater.*, 27 (2015) 2768–2774.
- [13] H. Zhang, H. Yang, H.J. Chen, X. Du, D. Wen, H. Wu, Photothermal conversion characteristics of gold nanoparticles under different filter conditions, *Energy*, 141 (2017) 32–39.
- [14] F. Tao, Y. Zhang, K. Yin, S. Cao, X. Chang, Y. Lei, D.S. Wang, R. Fan, L. Dong, Y. Yin, X. Chen, Copper sulfide-based plasmonic photothermal membrane for high-efficiency solar vapor generation, *ACS Appl. Mater. Interfaces*, 10 (2018) 35154–35163.
- [15] H. Liu, C. Chen, H. Wen, R. Guo, N.A. Williams, B. Wang, F. Chen, L. Hu, Narrow bandgap semiconductor decorated wood membrane for high-efficiency solar-assisted water purification, *J. Mater. Chem. A*, 6 (2018) 18839–18846.
- [16] X. Luo, C. Huang, S. Liu, J. Zhong, High performance of carbon-particle/bulk-wood bi-layer system for solar steam generation, *Int. J. Energy Res.*, 42 (2018) 4830–4839.
- [17] X. Tan, Y. Cheng, S. Wang, Design of interface-stable Janus solar-energy evaporator, *Int. J. Therm. Sci.*, 179 (2022) 107712, doi: 10.1016/j.ijthermalsci.2022.107712.
- [18] D. Fan, H. Min, H. Zhang, Y. Tang, X. Yang, Y. Lu, Architecting a bifunctional solar evaporator of perovskite $\text{La}_{0.5}\text{Sr}_{0.5}\text{CoO}_3$ for solar evaporation and degradation, *J. Mater. Sci.*, 56 (2021) 18625–18635.
- [19] H. Bai, P. He, L. Hao, Z. Fan, R. Niu, T. Tang, J. Gong, Waste-treating-waste: upcycling discarded polyester into metal-organic framework nanorod for synergistic interfacial solar evaporation and sulfate-based advanced oxidation process, *Chem. Eng. J.*, 456 (2023) 140994, doi: 10.1016/j.cej.2022.140994.
- [20] B. Zhu, H. Kou, Z. Liu, Z. Wang, D.K. Macharia, M. Zhu, B. Wu, X. Liu, Z. Chen, Flexible and washable CNT-embedded PAN nonwoven fabrics for solar-enabled evaporation and desalination of seawater, *ACS Appl. Mater. Interfaces*, 11 (2019) 35005–35014.
- [21] X. Liang, X. Zhang, Q. Huang, H. Zhang, C. Liu, Y. Liu, Simple preparation of external-shape and internal-channel size adjustable porous hydrogels by fermentation for efficient solar interfacial evaporation, *Sol. Energy*, 208 (2020) 778–786.
- [22] K. Bae, G. Kang, S.K. Cho, W. Park, K. Kim, W.J. Padilla, Flexible thin-film black gold membranes with ultrabroadband plasmonic nanofocusing for efficient solar vapour generation, *Nat. Commun.*, 6 (2015) 10103, doi: 10.1038/ncomms10103.
- [23] X. Li, W. Xu, M. Tang, L. Zhou, B. Zhu, S. Zhu, J. Zhu, Graphene oxide-based efficient and scalable solar desalination under one sun with a confined 2D water path, *Proc. Natl. Acad. Sci. U.S.A.*, 113 (2016) 13953–13958.
- [24] J.-T. Wang, J.-L. Hong, Effect of folding on 3D photothermal cones with efficient solar-driven water evaporation, *Appl. Therm. Eng.*, 178 (2020) 115636, doi: 10.1016/j.applthermaleng.2020.115636.
- [25] B. Henderson-sellers, A new formula for latent heat of vaporization of water as a function of temperature, *Q.J. R. Meteorol. Soc.*, 110 (1984) 1186–1190.
- [26] Z. Liu, H. Song, D. Ji, C. Li, A. Cheney, Y. Liu, N. Zhang, X. Zeng, B. Chen, J. Gao, Y. Li, X. Liu, D. Aga, S. Jiang, Z. Yu, Q. Gan, Extremely cost-effective and efficient solar vapor generation under nonconcentrated illumination using thermally isolated black paper, *Global Challenges*, 1 (2017) 1600003, doi: 10.1002/gch2.201600003.
- [27] Y. Xu, J. Ma, D. Liu, H. Xu, F. Cui, W. Wang, Origami system for efficient solar driven distillation in emergency water supply, *Chem. Eng. J.*, 356 (2019) 869–876.